Implementation of a new constitutive model for abdominal muscles

Lluís Tuset[a,*], Gerard Fortuny[a], Joan Herrero[b], Dolors Puigjaner[a], Josep M. López[a]

[a] *Departament d'Enginyeria Informàtica i Matemàtiques, Universitat Rovira i Virgili, Av Països Catalans 26, Tarragona, Catalunya, Spain*

[b] *Departament d'Enginyeria Química, Universitat Rovira i Virgili, Av Països Catalans 26, Tarragona, Catalunya, Spain*

Abstract

Background and objective: Abdominal hernia repair is one of the most often performed surgical procedures worldwide. Numerical simulations of the abdominal wall mechanics can be a valuable tool to devise actions aimed at preventing hernia formation. A first step towards this goal is the development of consistent constitutive models for the tissues that form the human abdominal wall. In this study we propose, for each of the tissues involved, a new formulation of the so–called transversely isotropic hyperelastic model (TIHM).

Methods: We propose a new TIHM for the human abdominal wall tissues and we present a systemic view of the methodology that we have implemented in the present study. First we consider the mathematical background of the TIHM. The novelty of our formulation is that both the isotropic and the fiber contributions to the strain energy function are characterized exclusively by polynomial convex functions of certain invariant quantities. Then, we provide a detailed description on how the constitutive model is implemented into an open source finite element (FE) software. In our approach we use the specific interface provided by the `MFront` software to incorporate our TIHM formulation into the `Code Aster` FE solver. For each of the tissues considered, the values of the TIHM constants are adjusted by means of a numerical simulation of previous experimental data from tensile tests.

Results: We studied the following abdominal wall tissues: linea alba, rectus sheath, external oblique muscle, internal oblique muscle, transversus abdominis muscle and rectus abdominis muscle. Our formulation, closely reproduces tensile test data for each tissue in

*corresponding author: Tel: +34 977559668; fax:+34 977559710

Email addresses: `lluis.tuset.serra@gmail.com` (Lluís Tuset), `gerard.fortuny@urv.cat` (Gerard Fortuny), `joan.herrero@urv.cat` (Joan Herrero), `dolors.puigjaner@urv.cat` (Dolors Puigjaner), `josep.m.lopez@urv.cat` (Josep M. López)

the corresponding FE numerical simulation.

Conclusions: The new TIHM formulation is suitable for a future numerical investigation of the abdominal wall, which will in turn help us to assess the best zone to practice a colostomy. The methodology implemented in the present study can be easily extended in the future to develop and implement a TIHM for active muscles and/or a different type of constitutive model which might be suitable to characterize other tissues of biomedical interest.

Keywords:

Abdominal wall, Open-source software, Strain energy functions, Hyperelasticity, Finite element method

1. Introduction

The study of the mechanical behavior of the abdominal wall is fundamental for the knowledge of the genesis of abdominal hernias. An abdominal hernia is a protrusion of the peritoneal sac through the muscular and aponeurotic set. Abdominal hernia repair is a quite common surgical operation. Actually, it is estimated that more than 20 million hernias are repaired throughout the world every year [1, 2]. In particular, more than 300 000 ventral hernia repairs and 700 000 inguinal hernia repairs were performed in 2003 in the USA[3]. Moreover, ventral hernia repairs are increasing at an estimated rate of 3% per year[3]. All these figures lead to a significant burden on the costs of healthcare systems. Therefore any action aimed at preventing hernia formation or improving hernia surgical interventions will be highly helpful.

The origin and recurrence of abdominal hernias are mostly still unknown today. Notwithstanding, it is known that a most common long–term complication following a colostomy is the creation of a hernia [4]. Therefore numerical simulations of the abdominal wall mechanics are a valuable tool to shed some light on this health problem. The abdominal wall is a composite of several muscles with different mechanical properties that contribute to its mechanical behavior [5]. Constitutive models of the different muscle tissues that form the abdominal wall play a key role in the simulations of its mechanics. The purpose of the current study is the development and implementation of a methodology that allows the simulation of the mechanical behavior of each type of muscle tissue and, moreover, to do so in

a computationally robust, transparent and efficient way.

A common physical model of the abdominal wall, which we assume in the present study, comprises the linea alba (LA), the two external oblique muscles (EO), the two internal oblique muscles (IO), the two transversus abdominis muscles (TR) and the two rectus abdominis muscle (RA). The model also considers the rectus-sheath (RS), which is a connective tissue made of collagen that encloses the RA. Soft tissues are usually modelled as hyperelastic materials [6], i.e., materials for which a strain energy function (SEF), also known as Helmholtz free-energy function, Ψ, is defined. If, in addition, the tissue is assumed to be slightly compressible then the SEF is decoupled into a volumetric and an isochoric part,

$$\Psi(J, \mathbf{C}) = U(J) + \Psi_{ich}(J, \mathbf{C}) \tag{1}$$

and the second Piola–Kirchoff stress tensor, $\mathbf{S}$, is consequently decoupled as,

$$\mathbf{S} = \mathbf{S}_{vol}(J) + \mathbf{S}_{ich}(J, \mathbf{C}) \tag{2}$$

where the volumetric and isochoric parts are defined as:

$$\mathbf{S}_{vol}(J) = 2\left(\frac{\partial U(J)}{\partial \mathbf{C}}\right) = 2U(J)_{,\mathbf{C}} \tag{3}$$

$$\mathbf{S}_{ich}(J, \mathbf{C}) = 2\left(\frac{\partial \Psi_{ich}(J, \mathbf{C})}{\partial \mathbf{C}}\right) = 2\Psi_{ich}(J, \mathbf{C})_{,\mathbf{C}} \tag{4}$$

In Eqs. (1–4) $\mathbf{C}$ denotes the right Cauchy–Green symmetric tensor, defined as $\mathbf{C} = \mathbf{F}^T\mathbf{F}$, where $\mathbf{F}$ is the deformation gradient and J is the determinant of $\mathbf{F}$. In Eqs. (3) and (4) the compact $()_{,\mathbf{C}}$ notation for the partial derivative of a tensor–valued function is introduced. At this point it is worth noting that the second Piola–Kirchoff strain tensor is the dual of the Green–Lagrange strain tensor and that the use of the right Cauchy–Green tensor $\mathbf{C}$ ensures objectivity (frame–independence).

To simulate the behavior of soft tissues such as those found in the abdominal wall it is necessary to consider anisotropy [7, 8], as fibers tend to have preferred directions and a non-linear behavior at large strains [9]. The so–called transversely isotropic hyperelastic model (TIHM) fulfills both theoretical requirements [6] and has been therefore frequently used to model soft tissue behavior. It is worth noting that the TIHM, as is the case with any purely elastic constitutive model, is not suited to predict short–term memory effects such as the

rate–induced hardening of pig skin reported by Zhou et al. [10]. One approach to model such effects consists in the addition of a viscous SEF into the r.h.s. of Eq. (1) [11]. Recently published proposals of the so–called transversely isotropic viscous–hyperelastic constitutive model may be found in Refs. [12–14].

In the TIHM, the soft tissue is assumed to be a composite formed by a ground isotropic material and one family of fibers which have a preferred direction, $\mathbf{a}_0$. It is customary to implement the constitutive equation (4) in terms of the modified SEF, $\overline{\Psi} = \overline{\Psi}(\overline{\mathbf{C}}, \mathbf{a}_0)$, where $\overline{\mathbf{C}} = J^{-2/3}\mathbf{C}$ is the modified right Cauchy–Green tensor:

$$\mathbf{S}_{ich}(J, \mathbf{C}, \mathbf{a}_0) = 2\Psi_{ich}(J, \mathbf{C}, \mathbf{a}_0)_{,\mathbf{C}} = 2\overline{\Psi}(\overline{\mathbf{C}}, \mathbf{a}_0)_{,\mathbf{C}} = 2\overline{\Psi}(\overline{\mathbf{C}}, \mathbf{a}_0)_{,\overline{\mathbf{C}}} : \overline{\mathbf{C}}_{,\mathbf{C}} = \overline{\mathbf{S}} : \mathbb{P} \tag{5}$$

The tensor quantities $\overline{\mathbf{S}}$ and $\mathbb{P}$ introduced in Eq. (5) are defined as [6]:

$$\overline{\mathbf{S}}(\overline{\mathbf{C}}, \mathbf{a}_0) = 2\overline{\Psi}(\overline{\mathbf{C}}, \mathbf{a}_0)_{,\overline{\mathbf{C}}} \tag{6}$$

$$\mathbb{P}(J, \mathbf{C}) = \overline{\mathbf{C}}_{,\mathbf{C}} = J^{-2/3}\left(\mathbb{I} - \frac{1}{3}\mathbf{C} \otimes \mathbf{C}^{-1}\right) \tag{7}$$

In Eq. (7), $\mathbb{I}$ denotes the fourth–order unit tensor. In practice, the rather expensive evaluation of the $\overline{\mathbf{S}} : \mathbb{P}$ double contraction in Eq. (5) can be circumvented using the following identity [15]:

$$\overline{\mathbf{S}} : \mathbb{P} = J^{-2/3}\left(\overline{\mathbf{S}} - \frac{1}{3}\left(\overline{\mathbf{S}} : \mathbf{C}\right)\mathbf{C}^{-1}\right) \tag{8}$$

In the TIHM formulation, a fibrous tissue is modeled by decomposing the modified SEF, $\overline{\Psi}$, into a ground isotropic contribution, $\overline{\Psi}_{iso}$, plus a fiber contribution, $\overline{\Psi}_{fib}$:

$$\overline{\Psi}(\overline{\mathbf{C}}, \mathbf{a_0}) = \overline{\Psi}_{iso}(\overline{\mathbf{C}}) + \overline{\Psi}_{fib}(\overline{\mathbf{C}}, \mathbf{a_0}) \tag{9}$$

Since the SEF must be independent of the coordinate system $\overline{\Psi}_{iso}$ and $\overline{\Psi}_{fib}$ are expressed as functions of invariants and pseudo–invariants of $\overline{\mathbf{C}}$ and $\mathbf{a}_0 \otimes \mathbf{a}_0$ [6]

$$\overline{\Psi}_{iso} = \overline{\Psi}_{iso}\left(\overline{I}_1(\overline{\mathbf{C}}), \overline{I}_2(\overline{\mathbf{C}})\right) \tag{10}$$

$$\overline{\Psi}_{fib} = \overline{\Psi}_{fib}\left(\overline{I}_4(\overline{\mathbf{C}}, \mathbf{a}_0), \overline{I}_5(\overline{\mathbf{C}}, \mathbf{a}_0)\right) \tag{11}$$

where

$$\overline{I}_1(\overline{\mathbf{C}}) = \mathrm{tr}(\overline{\mathbf{C}}) \tag{12}$$

$$\overline{I}_2(\overline{\mathbf{C}}) = \frac{1}{2}\left[\left(\mathrm{tr}(\overline{\mathbf{C}})\right)^2 - \mathrm{tr}\left(\overline{\mathbf{C}}^2\right)\right] \tag{13}$$

$$\overline{I}_4(\overline{\mathbf{C}}, \mathbf{a}_0) = \overline{\mathbf{C}} : (\mathbf{a}_0 \otimes \mathbf{a}_0) = \mathbf{a}_0^T \cdot \overline{\mathbf{C}} \cdot \mathbf{a}_0 = \lambda^2 \tag{14}$$

$$\overline{I}_5(\overline{\mathbf{C}}, \mathbf{a}_0) = \overline{\mathbf{C}}^2 : (\mathbf{a}_0 \otimes \mathbf{a}_0) = \mathbf{a}_0^T \cdot \overline{\mathbf{C}}^2 \cdot \mathbf{a}_0 \tag{15}$$

Note that the $\overline{I}_4$ pseudo–invariant has a direct physical interpretation as in Eq. (14) λ denotes the fiber stretching factor. As discussed in section 2.2 the convexity of a SEF is a valuable property to ensure the stability of the model. Let us recall that if a SEF depends on certain variables (invariants) and it is twice differentiable then its convexity is guaranteed if and only if its Hessian matrix is positive semidefinite.

In previous studies where a TIHM is proposed exponential functions of the invariants ($\overline{I}_1$,$\overline{I}_2$,$\overline{I}_4$,$\overline{I}_5$) are commonly used in the SEF formulation (see, for example, the review by Chagnon et al. [16]). In general, such exponential functions are found to describe well strong slope changes in the stress-strain curves. Notwithstanding, exponential functions have also been reported [17] to not always fit well experimental data for some strain ranges because of the exponential nature of the curves.

Narrowing the focus to abdominal wall tissues, Calvo et al. [18] adapted a TIHM previously formulated for the plantar fascia [19] to characterize the LA, RA, IO and EO of New Zealand White rabbits. Calvo et al.'s formulation was subseqently used by Grasa et al. [20] to simulate the passive response of the RA, EO and a multi-layered sample formed by EO, IO and TA. Calvo et al.'s model assumes a linear function of $\overline{I}_1$ for the isotropic part of SEF, Eq. (10), and a exponential function of $\overline{I}_4$ for the fiber contribution, Eq. (11). Pachera et al. [21] adapted a previous TIHM for arterial walls [22] to characterize the whole set of human abdominal tissues (LA, RS, RA, TR, IO and EO). In particular, Pachera et al.'s model uses a linear function of $\overline{I}_1$ in Eq. (10) and, depending on the particular tissue, either an exponential (LA, RS, RA and IO) or quadratic (EO and TR) function of $\overline{I}_4$ in Eq. (11).

The aim of the present study is the development of a new TIHM for the human abdominal wall tissues (LA, RS, RA, TR, IO and EO). In our model, the isotropic ($\overline{\Psi}_{iso}$) and fiber ($\overline{\Psi}_{fib}$) contributions to the SEF are characterized exclusively by polynomial functions of

the invariants of $\overline{\mathbf{C}}$ and $\mathbf{a}_0 \otimes \mathbf{a}_0$. Linear and exponential functions of the invariants do not provide, in some cases, a good enough fit to data because of too slow (linear) or too sudden (exponential) changes in the slope. Another good reason for adopting polynomial functions in the present study was the observation that in almost every available experimental studies the reported stress-strain curves of the tissues involved have a markedly polynomial look in the range of interest (typically $1 \leq \xi \leq 1.8$, where ξ denotes the stretch factor applied to the tissue sample).

From a methodological standpoint, we will perform numerical simulations of previously reported tensile tests [7, 23, 24] in order to determine the optimal values of the constitutive model parameters for each tissue. An additional objective of the present study is therefore an efficient implementation of the numerical problem that will allow us to perform a large number of runs with a limited amount of computational resources. In particular, we will pay attention to a both flexible and concise deployment of the constitutive model into the framework of a finite element (FE) software. Moreover, we will show that these methodological objectives can be achieved using free and open source software (FOSS). The FOSS packages available to tackle the present problem are not just inexpensive but powerful as well.

2. Material and methods

2.1. Constitutive model

Following the trend often observed in the literature [16] we first neglected the $\overline{I}_2$ and $\overline{I}_5$ invariants in Eqs. (10) and (11), respectively. After some preliminary numerical tests, we set the target on polynomial functions of the form:

$$\overline{\Psi}_{iso} = C_1 \left(\overline{I}_1 - 3\right) + C_2 \left(\overline{I}_1 - 3\right)^2 \tag{16}$$

$$\overline{\Psi}_{fib} = C_3 \left(\overline{I}_4 - 1\right)^2 + C_4 \left(\overline{I}_4 - 1\right)^4 \tag{17}$$

where C_i are positive constants. The quadratic form (16) was previously used by Raghavan and Vorp [25] as these authors found it to fit well data from uniaxially loaded tests on the wall of abdominal aortic aneurysms. The quartic function (17) was previously proposed by Peng et al. [26] as the fiber part of a SEF model for the human annulus fibrosus tissue. Note

that the $\overline{\Psi}_{iso}$ and $\overline{\Psi}_{fib}$ functions defined in Eqs. (16) and (17) are strictly convex functions of I_1 and I_4, respectively.

For the volumetric contribution to $\mathbf{S}$ in Eq. (3) we have used the following formulation:

$$U(J) = \frac{1}{2}K(J^2 - 1 - 2\ln J) \tag{18}$$

$$\mathbf{S}_{vol} = 2U(J)_{,\mathbf{C}} = U'J\mathbf{C}^{-1} = K\left(J^2 - 1\right)\mathbf{C}^{-1} \tag{19}$$

where $U' = \dfrac{dU}{dJ}$ and K is the bulk modulus. The particular form (18) for the volumetric function $U(J)$, proposed by Simo and Miehe's [27] as a refinement of Ogden's [28] model, relies on solid theoretical grounds and has become popular in the literature [29]. The isochoric–volumetric decoupling (2) is specially convenient when the constitutive model is implemented into a finite element (FE) nonlinear solver [16, 29] in order to avoid volumetric locking [30]. From a numerical standpoint, the volumetric contribution $\mathbf{S}_{vol}$ can be understood as a penalty function: the larger the value of K the smaller the volumetric strain $(J-1)$ will be.

Taking into account the identities [6],

$$\overline{I}_{1,\overline{\mathbf{C}}} = \mathbf{I} \quad ; \quad \overline{I}_{4,\overline{\mathbf{C}}} = \mathbf{a}_0 \otimes \mathbf{a}_0 \tag{20}$$

then for the SEF formulation (16-17) proposed in this study the particular form of $\overline{\mathbf{S}}$ (see Eqs. (6) and (9)) is given by:

$$\overline{\mathbf{S}} = \overline{\gamma}_1\mathbf{I} + \overline{\gamma}_4\mathbf{a}_0 \otimes \mathbf{a}_0 \tag{21}$$

$$\overline{\gamma}_1\left(\overline{I}_1\right) = 2\left(\frac{\partial\overline{\Psi}_{iso}}{\partial\overline{I}_1}\right) = 2C_1 + 4C_2(\overline{I}_1 - 3) \tag{22}$$

$$\overline{\gamma}_4\left(\overline{I}_4\right) = 2\left(\frac{\partial\overline{\Psi}_{fib}}{\partial\overline{I}_4}\right) = 4C_3(\overline{I}_4 - 1) + 8C_4(\overline{I}_4 - 1)^3 \tag{23}$$

2.2. Ellipticity of the governing equations

Some authors [18–20, 26] imposed the additional constraint that the fibers do not contribute to the SEF when they are under contraction:

$$\overline{\Psi}_{fib} = 0 \qquad \forall\, \overline{I}_4 < 1 \tag{24}$$

The Ψ_{fib} formulation (17) automatically fulfills the conditions

$$\overline{\Psi}_{fib}(1) = 0, \quad \left(\frac{\partial\overline{\Psi}_{fib}}{\partial\overline{I}_4}\right)(1) = 0, \quad \left(\frac{\partial^2\overline{\Psi}_{fib}}{\partial\overline{I}_4{}^2}\right)(1) \geq 0 \tag{25}$$

It is easy to show that the use of Eq. (17) also implies the additional conditions,

$$\frac{\partial \overline{\Psi}_{fib}}{\partial \overline{I}_4} > 0 (< 0) \quad \text{for} \quad \overline{I}_4 > 1 (< 1) \tag{26}$$

that is, some positive (negative) stress is actually to be exerted by a stretched (compressed) fiber. Note that the constraint (24) is incompatible with Eq. (26).

It is known that fibers tend to suffer failure mechanisms, such as fiber kinking or fiber splitting, when compressed. Merodio and Ogden [31] and Holzapfel et al. [22] analyzed the relation between the onset of such failure mechanisms and the loss of ellipticity of the governing equations in transversely isotropic elastic solids reinforced with a fiber contribution. These authors showed that, whenever a strictly convex function of $(\overline{I}_4 - 1)$ is prescribed, a necessary condition for the breakdown of ellipticity is that $\partial \overline{\Psi}_{fib} / \partial \overline{I}_4 < 0$, which means that the loss of ellipticity is to be expected under fiber compression $(\overline{I}_4 < 1)$.

Thus, it follows on account of (26) that whenever $\overline{\Psi}_{fib}$ is a strictly convex function of $\overline{I}_4$, as is the case of Eq. (17), the strong ellipticity of the governing equations is not guaranteed. This is probably the reason why several authors assume the constraint (24). In the present study we will apply Eq. (17) with no additional constraint. Note that Eq. (17) will be used, in the worst case scenario, with $\overline{I}_4$ values slightly below one. That is, when considering a tensile loading along a direction normal to the main fiber orientation the fibers will be somewhat compressed because of the (nearly) incompressibility of the material. In this situation ($\overline{I}_4$ slightly below one) the stability of the overall SEF model (9) may well be maintained even when the fiber contribution part alone would become unstable [31].

2.3. Tensile testing simulation

Tensile tests [7, 23, 24] are typically performed on a thin rectangular tissue sample, as sketched in Fig. 1. The tissue sample, having initially a length L_0, a width W_0 and a thickness H_0 (not shown in the sketch), is fixed on one lateral edge and is pulled on the opposite one. For every particular value of the external load applied (f), the stretch of the sample, ΔL, is measured.

2.3.1. Finite element simulation

The `Code Aster` open source FE software [32] was used in the present simulations. In the geometrical model the tissue sample was defined as a cuboid of dimensions $L_0 = 35$ mm,

Figure 1: Sketch of the model considered in the approximate analytical solution.

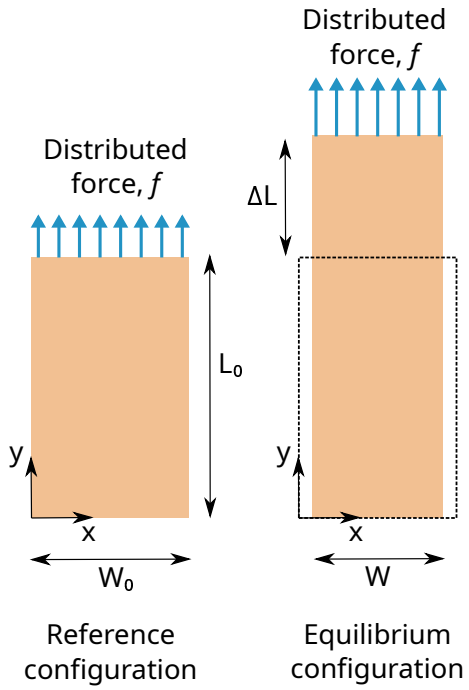

$W_0 = 10$ mm and $H_0 = 1$ mm. The computational meshes were created by first meshing the surfaces of the cuboid using isosceles and equilateral triangles and then generating the corresponding three-dimensional (3D) mesh of tetrahedra. Conditions of zero displacement and homogeneous stress level were imposed at the left and right $y-$boundaries, respectively (see Fig. 1). Fifty levels of the external load f, ranging from zero to the maximum prescribed value, were calculated on every computational run. For every particular load level, the resulting displacement at the right $y-$ boundary, ΔL, was recorded. The accuracy and computational performance of the present FE simulations are assessed in Appendix A.

2.3.2. Implementation details

The `Code Aster` FE software features a large number of built–in material behaviors and also allows the user the possibility to incorporate custom–made constitutive models. The `Code Aster` nonlinear solver was set to apply the FE discretization scheme of Simo and Miehe [27], which is well suited for large deformations. Since the resulting set of nonlinear equations was solved by means of the Newton method the contribution of the constitutive model to the global Jacobian has to be provided in the form of the fourth order tangent

tensor, $\mathbb{E}$:

$$\mathbb{E} = \mathbb{E}_{vol} + \mathbb{E}_{ich} = (\mathbf{S}_{vol})_{,\mathbf{C}} + (\mathbf{S}_{ich})_{,\mathbf{C}} \tag{27}$$

The contribution of the volumetric part to the Jacobian is given by,

$$\mathbb{E}_{vol} = (\mathbf{S}_{vol})_{,\mathbf{C}} = \frac{1}{2}\left(U''J^2 + U'J\right)\mathbf{C}^{-1}\otimes\mathbf{C}^{-1} - U'J\mathbf{C}^{-1}\odot\mathbf{C}^{-1} \tag{28}$$

where $U'' = \dfrac{d^2U}{dJ^2}$ and $(\mathbf{C}^{-1}\odot\mathbf{C}^{-1}) = -\mathbf{C}^{-1}{}_{,\mathbf{C}}$ [6]. The contribution of the isochoric part to the Jacobian is more involved:

$$\begin{aligned}
\mathbb{E}_{ich} &= \mathbb{P}^T : \overline{\mathbb{E}} : \mathbb{P} - \frac{1}{3}J^{-2/3}\left(\overline{\mathbf{S}}\otimes\mathbf{C}^{-1} + \mathbf{C}^{-1}\otimes\overline{\mathbf{S}}\right) + \\
&\quad + \frac{1}{3}\left(\overline{\mathbf{S}} : \overline{\mathbf{C}}\right)\left(\mathbf{C}^{-1}\odot\mathbf{C}^{-1} + \frac{1}{3}\mathbf{C}^{-1}\otimes\mathbf{C}^{-1}\right) && (29)\\
\overline{\mathbb{E}} &= \overline{\mathbf{S}}_{,\overline{\mathbf{C}}} && (30)
\end{aligned}$$

Considering Eqs. (19) and (21) then the particular forms of the fourth order tensors $\mathbb{E}_{vol}$ and $\overline{\mathbb{E}}$ for the present TIHM are:

$$\begin{aligned}
\mathbb{E}_{vol} &= K\left(J^2\mathbf{C}^{-1}\otimes\mathbf{C}^{-1} - \left(J^2-1\right)\mathbf{C}^{-1}\odot\mathbf{C}^{-1}\right) && (31)\\
\overline{\mathbb{E}} &= \overline{\delta}_1\mathbf{I}\otimes\mathbf{I} + \overline{\delta}_4\mathbf{a}_0\otimes\mathbf{a}_0\otimes\mathbf{a}_0\otimes\mathbf{a}_0 && (32)\\
\overline{\delta}_1\left(\overline{I}_1\right) &= \frac{\partial\overline{\gamma}_1}{\partial\overline{I}_1} = 4C_2 && (33)\\
\overline{\delta}_4\left(\overline{I}_4\right) &= \frac{\partial\overline{\gamma}_4}{\partial\overline{I}_4} = 4C_3 + 24C_4(\overline{I}_4 - 1)^2 && (34)
\end{aligned}$$

Figure 2: Sketch of the flow of data between the `Code Aster` and `MFront` programs.

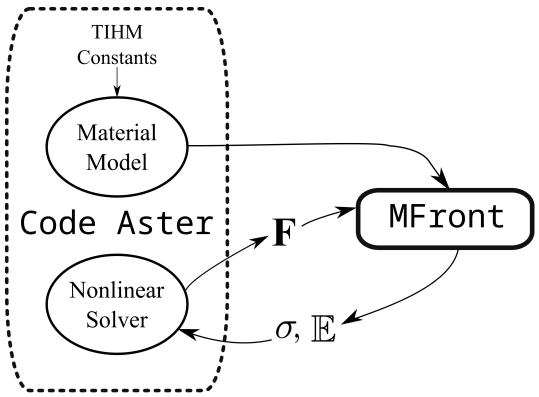

Table 1: Pseudocode illustrating the `MFront` calculation sequence for the present TIHM. The variables defined in the code are denoted using math symbols for the sake of clarity with the only exception of `F1`, which is the reserved word for $\mathbf{F}$. The keyword `Stensor` is a shortcut to the type (`C++` class) defined in the `MFront` library for the representation of symmetric second order tensors. The keyword `Stensor4` refers to the `MFront` type that represents the subset of fourth order tensors that can be defined by the tensor product ($\otimes$) of two symmetric second order tensors.

#	Variables	Equations	`MFront` expression
1	`Real` J	$\det(\mathbf{F})$	`det(F1)`
2	`Stensor` $\mathbf{C}$	$\mathbf{F}^T\mathbf{F}$	`computeRightCauchyGreenTensor(F1)`
3	`Stensor` $\mathbf{C}^{-1}$		`invert(C)`
4	`Real` $J^{-2/3}$		`pow(`J`,-2./3.)`
5	`Stensor` $\overline{\mathbf{C}}$	$J^{-2/3}\mathbf{C}$	$(J^{-2/3})$`*C`
6	`Stensor` $\mathbf{A}_0$	$\mathbf{a}_0 \otimes \mathbf{a}_0$	`buildFromVectorDiadicProduct(`$\mathbf{a}_0$`)`
7	`Real` $\overline{I}_1$	(12)	`trace(`$\overline{\mathbf{C}}$`)`
8	`Real` $\overline{I}_4$	(14)	$\overline{\mathbf{C}}$`|`$\mathbf{A}_0$
9	`Real` $\overline{\gamma}_1$	(22)	`2*`C_1`+4*`C_2`*(`$\overline{I}_1$`-3)`
10	`Real` $\overline{\gamma}_4$	(23)	`4*`C_3`*(`$\overline{I}_4$`-1)+8*`C_4`*pow(`$\overline{I}_4$`-1,3)`
11	`Real` $\overline{\delta}_1$	(33)	`4*`C_2
12	`Real` $\overline{\delta}_4$	(34)	`4*`C_3`+24*`C_4`*(`$\overline{I}_4$`-1)*(`$\overline{I}_4$`-1)`
13	`Stensor` $\overline{\mathbf{S}}$	(21)	$\overline{\gamma}_1$`*Stensor::Id()+`$\overline{\gamma}_4$`*`$\mathbf{A}_0$
14	`Stensor` $\mathbf{S}_{ich}$	(5)	$(J^{-2/3})$`*(`$\overline{\mathbf{S}}$`-(`$\overline{\mathbf{S}}$`|C)/3*`$\mathbf{C}^{-1}$`)`
15	`Stensor` $\mathbf{S}_{vol}$	(19)	K`*(`J`*`J`-1)*`$\mathbf{C}^{-1}$
16	`Stensor` $\boldsymbol{\sigma}$	(2), (37)	`convertSecondPiolaKirchoffStress toCauchyStress(`$\mathbf{S}_{vol}$`+`$\mathbf{S}_{ich}$`,F1)`
17	`Stensor4` $\mathbb{C}^{-1}_{\otimes}$	$\mathbf{C}^{-1} \otimes \mathbf{C}^{-1}$	$\mathbf{C}^{-1} \wedge \mathbf{C}^{-1}$
18	`Stensor4` $\mathbb{C}^{-1}_{\odot}$	(35)	`circledot(`$\mathbf{C}^{-1}$`)`
19	`Stensor4` $\mathbb{E}_{vol}$	(31)	K`*`J`*`J`*`$\mathbb{C}^{-1}_{\otimes}$`-`$K$`*(`$J$`*`$J$`-1)*`$\mathbb{C}^{-1}_{\odot}$
20	`Stensor4` $\overline{\mathbb{E}}$	(32)	$\overline{\delta}_1$`*(Stensor::Id()∧Stensor::Id())+`$\overline{\delta}_4$`*(`$\mathbf{A}_0 \wedge \mathbf{A}_0$`)`
21	`Stensor4` $\mathbb{P}$	(7)	$(J^{-2/3})$`*(Stensor4::Id()-(1./3.)*(`$\mathbf{C} \wedge \mathbf{C}^{-1}$`))`
22	`Stensor4` $\mathbb{P}^T$		$(J^{-2/3})$`*(Stensor4::Id()-(1./3.)*(`$\mathbf{C}^{-1} \wedge \mathbf{C}$`))`
23	`Stensor4` $\mathbb{E}_{ich}$	(29)	$\mathbb{P}^T$`*`$\overline{\mathbb{E}}$`*`$\mathbb{P}$`-(1./3.)*(`$J^{-2/3}$`)*(`$\overline{\mathbf{S}} \wedge \mathbf{C}^{-1}$`+`$\mathbf{C}^{-1} \wedge \overline{\mathbf{S}}$`)+ (1./3.)*(`$\overline{\mathbf{S}}$`|`$\overline{\mathbf{C}}$`)*(`$\mathbb{C}^{-1}_{\odot}$`+(1./3.)*`$\mathbb{C}^{-1}_{\otimes}$`)`
24	`Stensor4` $\mathbb{E}$	(27)	$\mathbb{E}_{vol}$ + $\mathbb{E}_{ich}$

As sketched in Fig. 2, in a custom implementation of a constitutive model into `Code Aster` the code supplied by the user will receive the gradient tensor $\mathbf{F}$ as an input argument and will return the calculated values of both $\mathbf{S}$ (or $\boldsymbol{\sigma}$) and $\mathbb{E}$ on exit. In the present study we used the specific interface provided by the `MFront` software [33] to incorporate the present TIHM into `Code Aster`. Besides its straightforward integration with `Code Aster` the most attractive feature of `MFront` is its elegant high–level language, especially suited for tensor algebra [34]. Hence, `MFront` provides a representation for second and fourth order tensors and most of their operations involved in the constitutive model equations. Table 1 shows the `MFront` code that we wrote for the present TIHM. Note that the code includes a call to the non–standard `circledot()` function (instruction # 18), written by ourselves in `C++`, that performs the tensor operation $\mathbf{C}^{-1} \odot \mathbf{C}^{-1} = -\mathbf{C}^{-1}{}_{,\mathbf{C}}$ based on the following equivalences [6] :

$$\begin{aligned} \mathbf{I} &= \mathbf{C}^{-1}\mathbf{C} \\ \mathbb{O} &= \mathbf{C}^{-1}{}_{,\mathbf{C}}\,\mathbf{C} + \mathbf{C}^{-1}\mathbf{C}_{,\mathbf{C}} = \mathbf{C}^{-1}{}_{,\mathbf{C}}\,\mathbf{C} + \mathbf{C}^{-1}\mathbb{I}^{s} \\ \mathbf{C}^{-1}{}_{,\mathbf{C}} &= -\mathbf{C}^{-1}\mathbb{I}^{s}\mathbf{C}^{-1} = -\mathbf{C}^{-1} \odot \mathbf{C}^{-1} \end{aligned} \tag{35}$$

In Eq. (35), $\mathbb{I}^{s}$ denotes a specialized symmetric version of the fourth order identity tensor [15]. A more computationally efficient, although far more convoluted as well, alternative for the calculation of the $\mathbb{P}^{T} : \overline{\mathbb{E}} : \mathbb{P}$ term in Eq. (29) is presented in Appendix B.

2.3.3. Approximate analytical solution

An approximate analytical model for the deformation of the tissue sample (see a sketch in Fig. 1) as a function of the applied external load f can be obtained as follows. First we assume that the load is homogeneously applied to the tissue sample lateral surface. Then assuming a small value of the volumetric strain $\Delta V/V$, that is, $J = (LWH)/(L_0W_0H_0) = 1+\Delta V/V \approx 1$, the deformation gradient tensor can be simplified to

$$\mathbf{F} = \begin{pmatrix} \lambda^{-1/2} & 0 & 0 \\ 0 & \lambda & 0 \\ 0 & 0 & \lambda^{-1/2} \end{pmatrix} \approx \begin{pmatrix} \xi^{-1/2} & 0 & 0 \\ 0 & \xi & 0 \\ 0 & 0 & \xi^{-1/2} \end{pmatrix} \tag{36}$$

where we have also assumed $\lambda \approx \xi = 1+\Delta L/L_0$. Note that Eq. (36) implies the assumptions $L = \xi L_0$, $W = \xi^{-1/2}W_0$ and $H = \xi^{-1/2}H_0$ for the deformation of the sample, that is, isotropy

is maintained in the $x - z$ plane.

In order to compare the stresses actually measured with the predicted ones we need to consider, in addition to the second Piola–Kichoff stress, $\mathbf{S}$, the Cauchy stress tensor, $\boldsymbol{\sigma}$,

$$\boldsymbol{\sigma} = J^{-1}\mathbf{F}\mathbf{S}\mathbf{F}^T \tag{37}$$

and the nominal stress tensor:

$$\boldsymbol{\Pi} = \mathbf{S}\mathbf{F}^T \tag{38}$$

The definition of the nominal stress tensor, $\boldsymbol{\Pi}$, is similar to that of the Cauchy stress except that it is expressed in terms of the area and normal of the surface in the reference configuration. Thus, $f/W_0H_0 = \Pi^{yy}$ is the quantity in our model that is to be compared with the experimental value since the nominal area, W_0H_0, is the one used to determine the measured stress level.

The simplified form (36) of the gradient tensor implies, on account of Eqs. (12) and (14), that $\overline{I}_1 = J^{-2/3}(\xi^2 + 2/\xi)$ and $\overline{I_4} = J^{-2/3}\xi^2$. Therefore, from Eqs. (5), (8), (19), (21) and (38) it follows, after some algebraic manipulation:

$$S^{yy} = S^{yy}_{vol} + S^{yy}_{ich} = \frac{K\left(J^2-1\right)}{\xi^2} + \frac{2}{3}J^{-2/3}\left(\left(1 - \frac{1}{\xi^3}\right)g_1(\xi) + g_4(\xi)\right) \tag{39}$$

$$\Pi^{yy} = \xi S^{yy} \tag{40}$$

$$g_1(\xi) = 2C_1 + 4C_2\left(J^{-2/3}\left(\xi^2 + \frac{2}{\xi}\right) - 3\right)$$

$$g_4(\xi) = 4C_3\left(J^{-2/3}\xi^2 - 1\right) + 8C_4\left(J^{-2/3}\xi^2 - 1\right)^3$$

We used Eqs. (39) and (40) in conjunction with the numerical simulations (described above) to determine the set of constants involved in the proposed THIM. Note that Eqs. (39) and (40) can be used to fit experimental data from tensile tests provided that a certain form is assumed for the variation of J with the sample stretch, ξ. Results from the numerical simulations suggested the use of a function of the type $J = 1 + a(\xi - 1)^3$, with $a = 0.10$.

The general approach to determine the constants K, C_1, C_2, C_3, and C_4 was to first obtain preliminary values of these constants by means of a nonlinear fit of the analytical model (39–40) to experimental data available in the literature. These preliminary values were subsequently refined by trial and error using the numerical simulations. Figure 3 illustrates

an instance for the deduction of the TIHM constants in the case of the TR muscle. In this figure we see that the analytical model (39–40) fits very well experimental data. However, this figure also shows that the preliminary set of constants does not perform so well in the numerical simulation which indicates that a following refinement of the constants is needed.

Figure 3: Example of the nonlinear fit of the present TIHM to previous data by Cardoso [23] for the TR muscle. The results of the preliminary numerical simulation, performed using the constants values given by the fit, are also plotted.

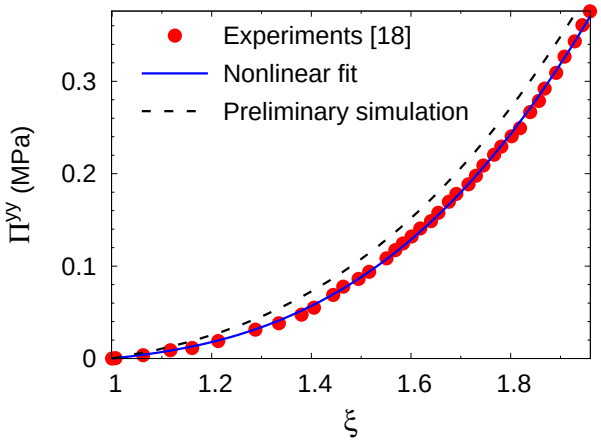

3. Results and discussion

We determined, for each of the tissues considered, the whole set of constants (K, C_1, C_2, C_3, C_4) involved in the proposed TIHM. It is worth noting that in the abdominal wall we can distinguish two types of materials, namely those basically composed of collagenous and aponeurotic tissues, such as LA and RS, and those that can be viewed as muscles, such as EO, IO, RA and TR. The former tissues deform much less than the latter ones when subjected to a certain external load. As the value of the bulk modulus, K, showed an enormous sensibility to changes in the objective function we had to fix suitable values for K. Numerical tests showed that $K = 100$ MPa worked well in the LA and RS simulations but a considerably smaller K value had to be used for the muscles. For the latter tissues we eventually chose $K = 1$ MPa, a value low enough to guarantee numerical stability of the simulations but high enough to maintain low levels of volumetric strain [35].

Figure 4: Results of the present simulations are compared with the measurements reported by Cardoso [23] on tissue samples of (a) TR, (b) EO, (c) IO and (d) RA. In all of the cases the tissue was stretched along the main direction of the fibers. Data from the same specimen in Cardoso's study is used in all of the four plots.

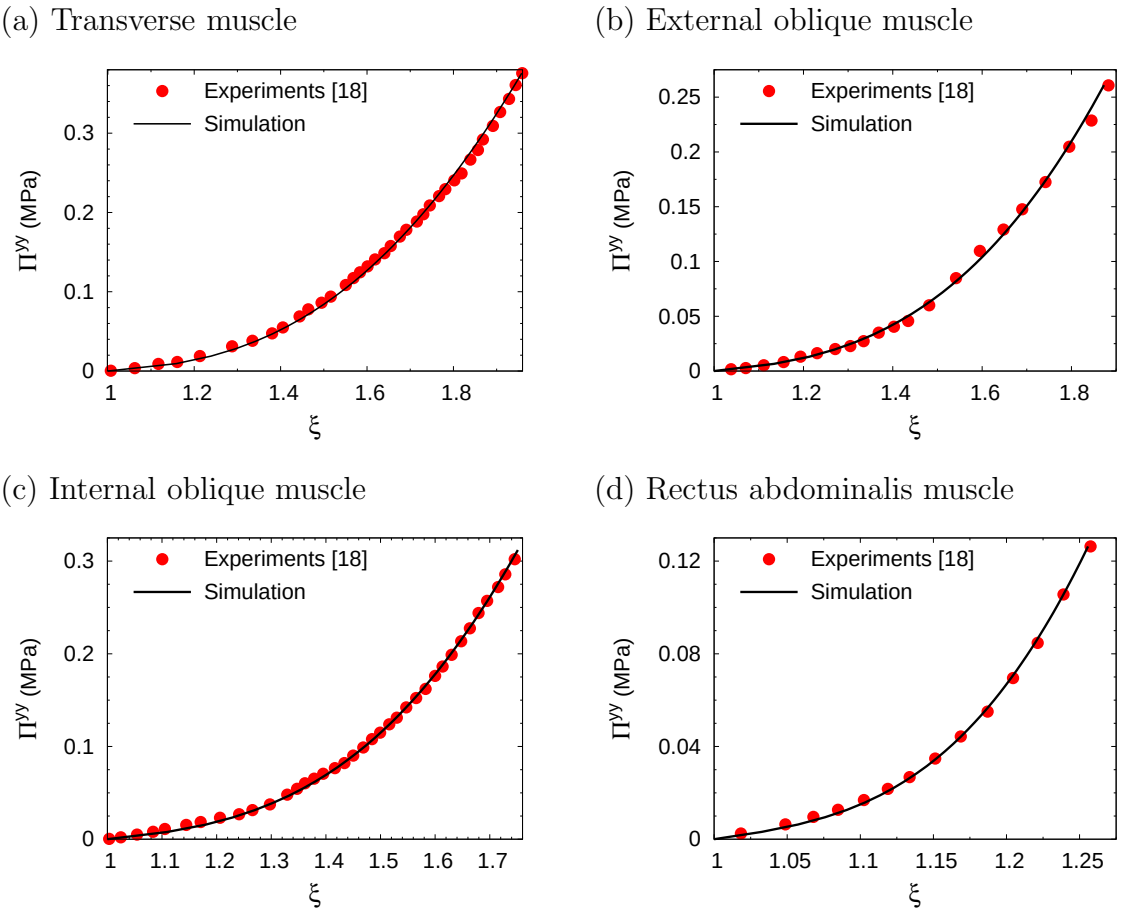

In the case of the EO, IO, RA and TR muscles we found that the C_1 values generated by the fits were very sensitive to small changes in the objective function. Therefore, we introduced the additional requirement that the final constant values of C_1 and C_3 had to be physically meaningful. Equations (39–40) predict that the slope of the stress–strain curve at the origin is $E_0 = \lim_{J,\xi\to 1} \partial\Pi^{yy}/\partial\xi = 4C_1 + 16C_3/3$, a result that was also validated by the numerical simulations. Thus, we required that the final values of C_1 and C_3 had to produce values of E_0 that were consistent with values typically reported in the literature for the elastic modulus of muscles at low strain levels [36]. In addition, in the trial and error adjustment we opted for a unique C_1 value for all of the four muscles. As a consequence of these additional

restrictions, in the present TIHM the isotropic contribution to the tissue response will be roughly the same for the four muscles when a low external load is applied.

Figure 4 (a) shows the comparison between experimental data and the results of the final simulations for the EO, IO, RA and TR muscles. For these four muscles we used the experimental data reported by Cardoso [23]. In all of the tensile tests performed by this author the tissue sample was only stretched along the main fiber direction. The final set of TIHM constants for every tissue are presented in Table 2. Note that from the respective C_1 and C_3 values in this table it can be checked that E_0 is within the $24-57$ kPa range for the EO, IO, RA and TR, a result that is in agreement with previously reported values [36].

Table 2: Values of the K, C_1, C_2, C_3 and C_4 constants in the present TIHM for every tissue of the abdominal wall

Tissue	K(MPa)	C_1(MPa)	C_2(MPa)	C_3(MPa)	C_4(MPa)
LA	100	0.05	11	0.1	34
RS			4.7	0.01	0.95
EO	1	0.0021	0.012	0.0029	0.00051
IO			0.016	0.0053	0.0015
RA			0.024	0.0092	0.052
TR			0.019	0.0031	0.00043

For the LA and RS we respectively fitted the experimental data reported by Forstemann et al. [7] and Martins et al. [24]. These authors carried out tensile tests were tissue samples were stretched either longitudinally (along the main fiber direction) and transversely. For these tissues, we first fitted transverse tests data to obtain preliminary values of C_1 and C_2 under the $C_3 = C_4 = 0$ constraint (no fiber contribution). These preliminary C_1 and C_2 values were set as constants in the fit of the corresponding longitudinal test data where preliminary C_3 and C_4 values were obtained. Numerical simulations were subsequently used to simultaneously refine the values of C_1, C_2, C_3 and C_4 for LA and RS. Figures 5 and 6 respectively compare experimental data and numerical results for the LA and RS tissues. The final values of the TIHM constants for LA and RS are shown in Table 2.

Figure 5: Results of the present simulations for the LA tissue are compared with the measurements reported by Forstemann et al. [7]. In parts (a) and (b) the main direction of the fiber alignment was respectively assumed to be parallel and normal to the direction along which the tissue sample was stretched.

(a) Parallel fiber orientation

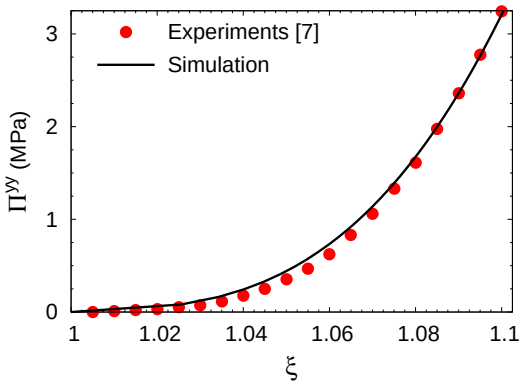

(b) Transverse fiber orientation

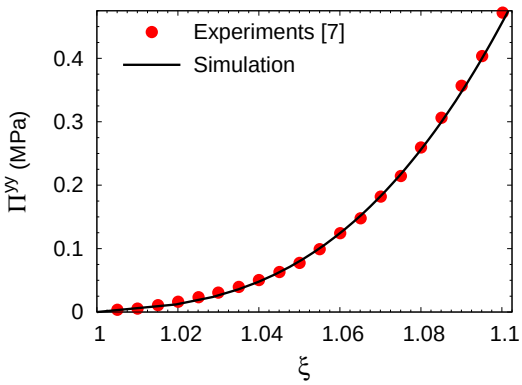

Figure 6: Results of the present simulations for the RS tissue are compared with the measurements reported by Martins et al. [24]. In parts (a) and (b) the main direction of the fiber alignment was respectively assumed to be parallel and normal to the direction along which the tissue sample was stretched. Data from the same specimen in Martins et al.'s study is used in both plots.

(a) Parallel fiber orientation

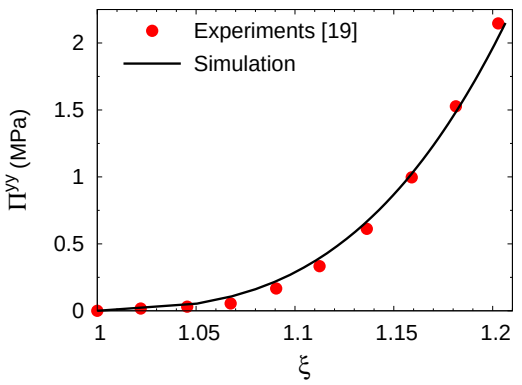

(b) Transverse fiber orientation

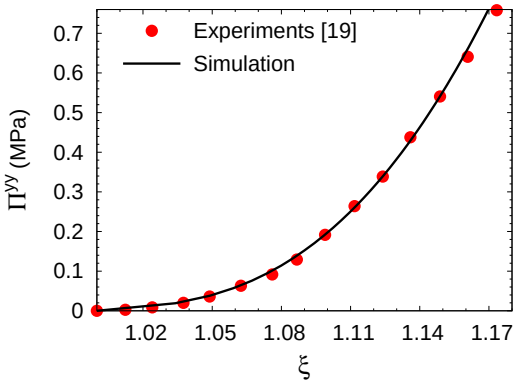

4. Conclusions

In this work we have developed a new constitutive TIHM formulation for tissues of the human abdominal wall. The present TIHM can be safely used to simulate problems in which tissues are being stretched with stress levels up to $\sigma = 0.2$ MPa. This is a wide enough range of application for the intended future use of the model, i.e., FE simulations of the abdominal wall where the maximum loads applied will be about $\sigma = 0.025$ MPa [21]. If higher stress values were to be applied the resulting large deformations ($\lambda > 2$) would render the FE simulation not only physically unreliable but, most probably, numerically unstable as well. In this respect, TIHM formulations using exponential functions of the invariants might be more numerically resilient (as the slope of the stress–strain curve tends to infinity large increases in σ would produce no further deformation of the material) but they might yield unrealistic predictions when used beyond their range of validity.

As was discussed above, under strong compression ($\overline{I}_4 \ll 1$) the present TIHM might produce a failure of the FE calculation. In previous TIHM formulations such a failure would be avoided by imposing the constraint (24) as a workaround. Our point of view is that under conditions where the real fibers would split it is preferable to obtain a breakage of the FE calculation rather than a physically meaningless numerical solution.

In the present study we have exclusively relied on open source software such as `MFront` and `Code Aster`. There are of course alternative methods to incorporate a custom material model into FE solvers but we think that as MFront provides a large number of tensorial operations its usage significantly eases the implementation of complex orthotropic finite strain behaviors. It is worth mentioning that `MFront` provides specific interfaces not only to `Code Aster` but to several other open source and commercial FE solvers as well.

A future application of the present TIHM will be in the analysis of the stress map on the abdominal wall in order to determine the best zone to practice a colostomy. As a preliminary step, we have also tested the present TIHM in the simulation of larger structures of the abdominal wall. As an example, Fig. 7 shows the predicted distribution of the longitudinal deformation (Δz) in the simulations of the right RA muscle under two different levels of vertical load, namely 5 kPa (left plot) and 10 kPa (right plot).

We have hitherto considered the passive response of the abdominal muscles under an

Figure 7: Vertical (z) component of the predicted deformation on the surface of the right RA muscle. The 3D mesh used in this simulation, consisting of 310 497 tetrahedra, was generated from a surface mesh consisting of 65 188 triangles. The dimensions of the bounding box surrounding the right RA model are 0.0762 m $\times$ 0.0727 m in the $x-y$ (horizontal) plane and 0.394 m in the z (vertical) direction. The boundary conditions in these simulations were roughly equivalent to the ones prescribed earlier for the rectangular tissue sample (see Fig. 1); that is, the right RA model was fixed at the bottom edge ($\Delta z = 0$) and a uniform stress load of either (a) 5 kPa (left) or (b) 10 kPa (right) was applied to the upper edge boundaries. The muscle fibers were assumed to be initially aligned with the $z-$axis.

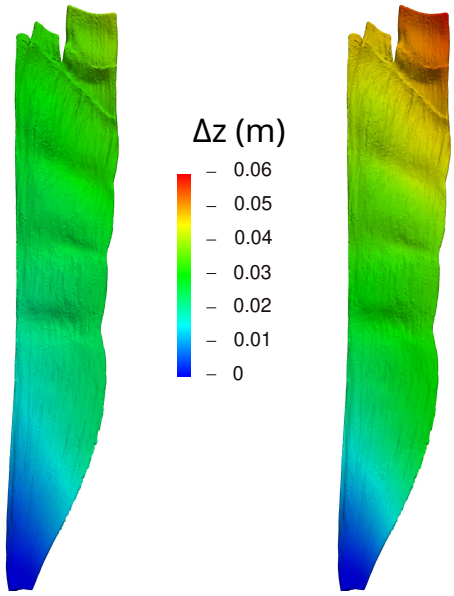

external load. A future goal will be the implementation of the current TIHM into a broader formulation able to simulate the action of active muscles (see, e.g., Refs. [37] and [38]). Future variations of the present TIHM might be developed for other tissues beyond the abdominal wall. Such future models might incorporate additional functions of the $\overline{I}_2$ and $\overline{I}_5$ invariants if a comprehensive enough experimental database was available for the tissues involved. The increased mathematical complexity of a new TIHM would imply an additional effort for its efficient implementation into the FE solver. At this point we would benefit of one of the main features of the current methodology as is the use of the `MFront` software, a both flexible and powerful tool.

Conflict of Interests

The authors declare that there is no conflict of interests regarding the publication of this paper.

Acknowledgement

Financial support for the current research was granted by Universitat Rovira i Virgili, project number 2018PFR-URV-B2-29.

[1] A. Kingsnorth, K. LeBlanc, Hernias: Inguinal and incisional, Lancet 362 (9395) (2003) 1561–1571.

[2] F. Köckerling, M. Simons, Current concepts of inguinal hernia repair, Visceral Medicine 34 (2) (2018) 145–150.

[3] C. Beadles, A. Meagher, A. Charles, Trends in emergent hernia repair in the united states, JAMA Surgery 150 (3) (2015) 194–200.

[4] S. Gillern, J. I. S. Bleier, Parastomal hernia repair and reinforcement: The role of biologic and synthetic materials, Clin. Colon Rectal Surg. 27 (4) (2014) 162–171.

[5] M. Kirilova, S. Stoytchev, D. Pashkouleva, V. Kavardzhikov, Experimental study of the mechanical properties of human abdominal fascia, Medical engineering & physics 33 (1) (2011) 1–6.

[6] G. A. Holzapfel, et al., Biomechanics of soft tissue, The handbook of materials behavior models 3 (2001) 1049–1063.

[7] T. Förstemann, J. Trzewik, J. Holste, B. Batke, M. Konerding, T. Wolloscheck, C. Hartung, Forces and deformations of the abdominal wall—a mechanical and geometrical approach to the linea alba, Journal of Biomechanics 44 (4) (2011) 600–606.

[8] D. Gräβel, A. Prescher, S. Fitzek, D. G. v. Keyserlingk, H. Axer, Anisotropy of human linea alba: A biomechanical study, Journal of Surgical Research 124 (1) (2005) 118–125.

[9] A. E. Ehret, M. Itskov, A polyconvex hyperelastic model for fiber-reinforced materials in application to soft tissues, Journal of Materials Science 42 (21) (2007) 8853–8863.

[10] B. Zhou, F. Xu, C. Q. Chen, T. J. Lu, Strain rate sensitivity of skin tissue under thermomechanical loading, Phil. Trans. R. Soc. A 368 (2010) 679–690.

[11] A. Voger, L. Rakotomanana, D. P. Pioletti, Viscohyperelastic strain energy function, in: Y. Payan, J. Ohayon (Eds.), Biomechanics of Living Organs. Hyperelastic Constitutive Laws for Finite Element Modeling, Academic Press Series in Biomedical Engineering, Academic Press, 2017, pp. 59–78.

[12] S. G. Kulkarni, X.-L. Gao, S. E. Horner, R. F. Mortlock, J. Q. Zheng, A transversely isotropic visco-hyperelastic constitutive model for soft tissues, Mathematics and Mechanics of Solids 21 (6) (2016) 747–770.

[13] A.-A. K. Yousefi, M. A. Nazari, P. Perrier, M. S. Panahi, Y. Payan, A visco-hyperelastic constitutive model and its application in bovine tongue tissue, Journal of Biomechanics 71 (2018) 190–198.

[14] D. Garcia-Gonzalez, A. Jérusalem, S. Garzon-Hernandez, R. Zaera, A continuum mechanics constitutive framework for transverse isotropic soft tissues, Journal of the Mechanics and Physics of Solids 112 (2018) 209–224.

[15] M. Itskov, Tensor Algebra and Tensor Analysis for Engineers, With Applications to Continuum Mechanics, 4th Edition, Mathematical Engineering, Springer, 2015.

[16] G. Chagnon, M. Rebouah, D. Favier, Hyperelastic energy densities for soft biological tissues: a review, Journal of Elasticity 120 (2) (2015) 129–160.

[17] B. Hernández-Gascón, E. Peña, H. Melero, G. Pascual, M. Doblaré, M. Ginebra, J. Bellón, B. Calvo, Mechanical behaviour of synthetic surgical meshes: finite element simulation of the herniated abdominal wall, Acta biomaterialia 7 (11) (2011) 3905–3913.

[18] B. Calvo, M. Sierra, J. Grasa, M. Munoz, E. Peña, Determination of passive viscoelastic response of the abdominal muscle and related constitutive modeling: Stress-relaxation behavior, Journal of the mechanical behavior of biomedical materials 36 (2014) 47–58.

[19] A. Natali, P. Pavan, E. Carniel, M. Lucisano, G. Taglialavoro, Anisotropic elasto-damage constitutive model for the biomechanical analysis of tendons, Medical engineering & physics 27 (3) (2005) 209–214.

[20] J. Grasa, M. Sierra, N. Lauzeral, M. Munoz, F. Miana-Mena, B. Calvo, Active behavior of abdominal wall muscles: Experimental results and numerical model formulation, Journal of the mechanical behavior of biomedical materials 61 (2016) 444–454.

[21] P. Pachera, P. Pavan, S. Todros, C. Cavinato, C. Fontanella, A. Natali, A numerical investigation of the healthy abdominal wall structures, Journal of biomechanics 49 (9) (2016) 1818–1823.

[22] G. A. Holzapfel, T. C. Gasser, R. W. Ogden, Comparison of a multi-layer structural model for arterial walls with a fung-type model, and issues of material stability, Journal of Biomechanical Engineering 126 (2004) 264–275.

[23] M. H. S. Cardoso, Experimental study of the human anterolateral abdominal wall. Biomechanical properties of fascia and muscles, Ph.D. thesis, Faculdade de Engenharia, Universidade do Porto (2012).

[24] P. Martins, E. Peña, R. N. Jorge, A. Santos, L. Santos, T. Mascarenhas, B. Calvo, Mechanical characterization and constitutive modelling of the damage process in rectus sheath, Journal of the mechanical behavior of biomedical materials 8 (2012) 111–122.

[25] M. L. Raghavan, D. A. Vorp, Toward a biomechanical tool to evaluate rupture potential of abdominal aortic aneurysm: identification of a finite strain constitutive model and evaluation of its applicability, Journal of Biomechanics 33 (2000) 475–482.

[26] X. Q. Peng, Z. Y. Guo, M. B., An anisotropic hyperelastic constitutive model with fiber–matrix shear interaction for the human annulus fibrosus, Journal of Applied Mechanics 73 (2006) 815–824.

[27] J. Simo, C. Miehe, Associative coupled thermoplasticity at finite strains: Formulation, numerical analysis and implementation, Computer Methods in Applied Mechanics and Engineering 98 (1) (1992) 41–104.

[28] R. W. Ogden, Large deformation isotropic elasticity–on the correlation of theory and experiment for incompressible rubberlike solids, Proc. R. Soc. Lond. A 326 (1567) (1972) 565–584.

[29] S. Doll, K. Schweizerhof, On the development of volumetric strain energy functions, Journal of Applied Mechanics 67 (2000) 17–21.

[30] T. Belytschko, W. K. Liu, B. Moran, K. I. Elkhodary, Nonlinear Finite Elements for Continua and Structures, 2nd Edition, Wiley, 2014.

[31] J. Merodio, R. W. Ogden, Instabilities and loss of ellipticity in fiber–reinforced compressible non–linearly elastic solids under plane deformation, International Journal of Solids and Structures 40 (2003) 4707–4727.

[32] code Aster, Structures and thermomechanics analysis for studies and research, https://www.code-aster.org/spip.php?rubrique2. Accessed 26-Feb-2019 (2019).

[33] MFront, A code generation tool dedicated to material knowledge, http://tfel.sourceforge.net/. Accessed 26-Feb-2019 (2019).

[34] T. Helfer, B. Michel, J.-M. Proix, M. Salvo, J. Sercombe, M. Casella, Introducing the open-source mfront code generator: Application to mechanical behaviours and material knowledge management within the pleiades fuel element modelling platform, Computers & Mathematics with Applications 70 (5) (2015) 994–1023.

[35] S. Aritan, S. O. Oyadiji, R. M. Bartlett, The *in vivo* mechanical properties of muscular bulk tissue, in: 31st Annual International Conference of the IEEE EMBS, 2009, pp. 5259–5262.

[36] K. M. M. Lima, J. F. S. Costa Júnior, W. C. A. Pereira, L. F. de Oliveira, Assessment of the mechanical properties of the muscle–tendon unit by supersonic shear wave imaging elastography: a review, Ultrasonography 37 (1) (2018) 3–15.

[37] A. E. Ehret, M. Böl, M. Itskov, A continuum constitutive model for the active behaviour of skeletal muscle, Journal of the Mechanics and Physics of Solids 59 (3) (2011) 625–636.

[38] P. G. Pavan, S. Todros, P. Pachera, S. Pianigiani, A. N. Natali, The effects of the muscular contraction on the abdominal biomechanics: a numerical investigation, Computer Methods in Biomechanics and Biomedical Engineering 22 (2) (2019) 139–148.

Appendix A. Accuracy and performance assessment of the finite element method

Table A.1: Accuracy and computational efficiency of FE calculations for the simulations of two different tissue samples (LA and TR) on four different computational meshes. N_{tet} denotes the number of tetrahedra in the computational mesh, MB_{max} is the maximum virtual memory (MB) reserved by the `Code Aster` software, ΔL_{max} is the calculated (absolute) stretch of the sample at maximum load, N_{iter} is the total number of Newton iterations performed, N_{solve} is the total number of solves during the whole calculation and T_{cpu} and T_{wall} respectively denote the elapsed CPU and wall time. These simulations were performed on a Intel Core i5-6600 CPU (Skylake-S) Quad Core with a maximum clock speed of 3900 MHz.

N_{tet}	662	1 819	4 164	7 789
MB_{max}	629	645	709	756
LA (fiber direction)				
ΔL_{max}(mm)	3.476	3.511	3.537	3.536
N_{iter}	443	487	438	444
N_{solve}	122	122	122	122
T_{cpu}(s)	16.21	35.36	68.53	127.44
T_{wall}(s)	9.42	25.05	51.85	99.07
T_{cpu}(s)/N_{iter}	0.037	0.073	0.156	0.287
TR				
ΔL_{max}(mm)	33.324	33.625	33.747	33.756
N_{iter}	777	758	1 020	842
N_{solve}	122	122	122	126
T_{cpu}(s)	27.16	53.31	151.34	231.30
T_{wall}(s)	15.36	37.36	112.54	177.57
T_{cpu}(s)/N_{iter}	0.035	0.070	0.148	0.275

Table A.1 shows the dependence of the accuracy and computational efficiency on the mesh size for simulations on two different abdominal tissues, namely LA and TR. In the case of the LA simulations, the calculated deformations are much smaller than they are in the TR runs so that the total number of Newton iterations is, for a given mesh size, significantly

lower in the former simulations. The total number of solves (N_{solve}) was actually higher than the number of scheduled load levels (50) as the FE solver implemented an adaptive step strategy that ensured the convergence of the Newton iterations on every particular instance. As expected, the total CPU time (T_{cpu}) required to complete a simulation run increases with increasing mesh size (N_{tet}). The FE solver was allowed to use 2 CPU cores in the simulations but the paralellization efficiency factor was modest, about 70% on the average. The `Code Aster` software used parallel code during the stage of matrix factorization, which in the present problem is relatively fast due to the regularity of the computational mesh. For the same reason, the average CPU time per Newton iteration (T_{cpu}/N_{iter}) is roughly proportional to the mesh size. That is, the matrix representation of the Jacobian tensor is not just sparse but most probably features a well defined structure (bands/blocks), easily amenable to the direct solver factorization algorithms implemented in `Code Aster`.

Table A.1 also shows that the calculated maximum deformations (ΔL_{max}) are almost identical for the two larger computational meshes whereas the relative numerical error at maximum load conditions in the mesh with $N_{tet} = 1\,819$ is 0.71% and 0.39% for the LA and TR runs, respectively. The computational mesh with 1 819 tetrahedra was subsequently adopted in the remainder of the simulations as a compromise between numerical accuracy and computational cost.

Appendix B. An optimized version of the `MFront` code for the present TIHM

The `MFront` code described in Table 1 relies on a rather straightforward implementation of the constitutive equations and can therefore be easily generalized to other variants of the TIHM. Notwithstanding, we found that the bottleneck in computational efficiency was in instruction #23 where two double contractions between fourth–order tensors ($\mathbb{P}^T : \overline{\mathbb{E}} : \mathbb{P}$) were involved. A more efficient version of the `MFront` code is based on the following expansion, derived from the combination of Eqs. (7) and (32):

$$\begin{aligned}\mathbb{P}^T : \overline{\mathbb{E}} : \mathbb{P} = \frac{1}{9}\left(\overline{\delta}_1 \overline{I}_1^2 + \overline{\delta}_4\, \overline{I}_4^2\right) \mathbb{C}_{\otimes}^{-1} + \overline{\delta}_1 J^{-4/3}\left(\mathbf{I}\otimes\mathbf{I}\right) + \overline{\delta}_4 J^{-4/3}\left(\mathbf{a}_0\otimes\mathbf{a}_0\otimes\mathbf{a}_0\otimes\mathbf{a}_0\right) - \\ - \frac{1}{3}\overline{\delta}_1 \overline{I}_1 J^{-2/3}\left(\mathbf{I}\otimes\mathbf{C}^{-1} + \mathbf{C}^{-1}\otimes\mathbf{I}\right) - \\ - \frac{1}{3}\overline{\delta}_4 \overline{I}_4 J^{-2/3}\left((\mathbf{a}_0\otimes\mathbf{a}_0)\otimes\mathbf{C}^{-1} + \mathbf{C}^{-1}\otimes(\mathbf{a}_0\otimes\mathbf{a}_0)\right) \quad \text{(B.1)}\end{aligned}$$

Table B.1 describes the modifications that were introduced into the original `MFront` code to implement Eq. (B.1).

Table B.1: Pseudocode illustrating the changes introduced in the `MFront` original code, presented in Table 1, to obtain the more efficient formulation based on Eq. (B.1). Instructions $\#1-19$, not included here, would be the same ones listed in Table 1.

#	Variables	Equations	`MFront` expression

20	`Stensor4` $\mathbb{P}^T$:$\overline{\mathbb{E}}$:$\mathbb{P}$	(B.1)	`(1./9.)*(`$\overline{\delta}_1$`*`$\overline{I}_1$`*`$\overline{I}_1$`+`$\overline{\delta}_4$`*`$\overline{I}_4$`*`$\overline{I}_4$`)*`$\mathbb{C}_{\otimes}^{-1}$`+`
			`(`$\overline{\delta}_1$`*`$J^{-2/3}$`*`$J^{-2/3}$`)*(Stensor::Id()`$\wedge$`Stensor::Id())`
			`+(`$\overline{\delta}_4$`*`$J^{-2/3}$`*`$J^{-2/3}$`)*(`$\mathbf{A}_0\wedge\mathbf{A}_0$`)`
			`-(1./3.)*(`$\overline{\delta}_1$`*`$\overline{I}_1$` *`$J^{-2/3}$`)*(Stensor::Id()`$\wedge\mathbf{C}^{-1}$
			`+`$\mathbf{C}^{-1}\wedge$`Stensor::Id())`
			`-(1./3.)*(`$\overline{\delta}_4$`*`$\overline{I}_4$`*`$J^{-2/3}$`)*(`$\mathbf{A}_0\wedge\mathbf{C}^{-1}+\mathbf{C}^{-1}\wedge\mathbf{A}_0$`)`

21	`Stensor4` $\mathbb{E}_{ich}$	(29)	$\mathbb{P}^T$:$\overline{\mathbb{E}}$:$\mathbb{P}$`-(1./3.)*(`$J^{-2/3}$`)*(`$\overline{\mathbf{S}}\wedge\mathbf{C}^{-1}+\mathbf{C}^{-1}\wedge\overline{\mathbf{S}}$`)+` `(1./3.)*(`$\overline{\mathbf{S}}\,|\,\overline{\mathbf{C}}$`)*(`$\mathbb{C}_{\odot}^{-1}$`+(1./3.)*`$\mathbb{C}_{\otimes}^{-1}$`)`
22	`Stensor4` $\mathbb{E}$	(27)	$\mathbb{E}_{vol}$ `+` $\mathbb{E}_{ich}$